ELSEVIER

Contents lists available at ScienceDirect

Composites Science and Technology

journal homepage: www.elsevier.com/locate/compscitech





Experimental and numerical investigations on the tensile response of pin-loaded carbon fibre reinforced polymer straps

Danijela Stankovic ^{a,b,c,*}, James R. Davidson ^b, Valentin Ott ^c, Luke A. Bisby ^a, Giovanni P. Terrasi ^c

- a Institute for Infrastructure & Environment, School of Engineering, University of Edinburgh, Mayfield Road, Edinburgh, EH9 3JL, UK
- b Department of Materials Science & Engineering, Faculty of Engineering, University of Sheffield, Sir Robert Hadfield Building, Mappin Street, Sheffield, S1 3JD, UK
- ^c Empa, Swiss Federal Laboratories for Materials Science and Technology, Uberland Str. 129, 8600, Dubendorf, Switzerland

ARTICLE INFO

Keywords:
Optical fibres
Carbon fibres
Failure criterion
Finite element analysis (FEA)
Elastic properties

ABSTRACT

Carbon fibre reinforced polymer (CFRP) pin-loaded looped straps are increasingly being used in a range of structural load-bearing applications, notably for bridge hanger cables in network arch rail and highway bridges. The static performance of such CFRP straps is investigated through experimental and numerical analyses. Finite element (FE) models based on both one-eighth and half pin-strap assembly geometries were modelled. The resulting strains, stresses, and applied loads were compared against experimental data obtained using Digital Image Correlation, Distributed Fibre Optic Sensing (DFOS), and Fibre Bragg Grating (FBG) Sensing. The FE models effectively captured local strain distributions around the vertex area, close to the pin ends of the straps, as well as in the mid-shaft region, and aligned reasonably with experimental observations. The half FE model accurately predicted the overall strain distribution when compared to DFOS data; however, higher strain magnitudes (by 0.45–10.2 %) and larger strain reductions were observed in some locations. Regarding failure loads, the FE models agreed well with Schürmann's analytical solution and the maximum stress criterion, exhibiting less than 2.5 % deviations from the experimental data. Furthermore, the predicted onset of strap failure (by delamination) in the half model agreed with experimental values, with a maximum variance of 9.2 %.

1. Introduction

Many criteria, methods, and equations exist for predicting the loadat-failure or damage accumulation processes of fibre reinforced polymer composite structural components. The response of unidirectional (UD) plies and laminated panels under static tensile loading-e.g. fibrematrix interactions, strength, stress states/redistributions, and fracture toughness—have all been systematically reported by various researchers e.g. Refs. [1-4]. Considering fibre-direction mechanical properties for unidirectional composites, fibre-failure is typically the dominant failure mode, often resulting in sudden brittle rupture (when loaded in tension) [5]. For this reason, simple strength-based failure criteria, such as the maximum stress/strain criterion, can often adequately predict failure loads in UD composite specimens, where reinforcing fibres are closely aligned with the principal loading direction [6]. However, to address more complex loading scenarios, layups, and geometries (typical in a range of industrial and construction applications), Hashin [7] and Puck [8] studied damage mechanisms considering more complex three dimensional stress states, alongside fibre and polymer matrix failure. Both proposed strength-based approaches that are interactive (allow stress redistribution) and can predict separate/dominant damage modes in fibre reinforced polymers. Subsequent researchers have developed more advanced methods, including a set of three-dimensional failure criteria for laminated fibre reinforced composites (termed "LaRCO4"), which further consider matrix-failure in tension. This approach uses physical models to describe each failure mode, and incorporates non-linear matrix shear behaviour [9].

Alternative methodologies for predicting failure in unidirectional (UD) members are outlined in by several authors [4,10–12]. Orifici et al. [10] presented failure (strength) theories for in-plane and interlaminar failure (damage onset), and employed classical fracture mechanics approaches to describe damage progression. In their study of failure modes in UD carbon fibre-reinforced polymer (CFRP) laminates, constructed from multiple layers of UD pre-impregnated tape, Orifici et al. found that failure typically occurred in a plane parallel to the fibre direction. Fibre failure was observed along the ply-fibre axis, whilst matrix failure

^{*} Corresponding author. Institute for Infrastructure & Environment, School of Engineering, University of Edinburgh, Mayfield Road, Edinburgh, EH9 3JL, UK. *E-mail address:* d.stankovic.davidson@sheffield.ac.uk (D. Stankovic).

occurred both along the fibre axis (via fibre bridging) and perpendicular to it. In most cases, the final failure observed in tensile tests was explosive rupture and could also be observed in UD specimens that were not necessarily flat, such as looped elements or straps.

The earliest numerical study on pin-loaded FRP straps, wherein CFRP tapes are wound continuously around metallic or composite pins at each end to create a pin-loaded continuous FRP strap system (an example of which is shown in Fig. 1), was conducted by Wörndle and Daschner [13] who used FE models and large deformation theory to estimate the distributions of tensile (and compressive) tangential stresses in looped straps made of glass, aramid, and carbon fibres (T300A fibres, Thornel 75S fibres). They considered symmetry conditions and analysed half of the pin/strap assembly under a plane stress state, assuming frictionless contact between the loading pin and the strap. Various outer-to-inner radius ratios were investigated, revealing that the highest stresses on the strap were concentrated at the edge in contact with the pin (referred to as the "vertex" in the current paper). Their primary findings indicated that a smaller outer-to-inner radius ratio correlated with an increased load-bearing capacity of the straps [13].

Schürmann [11] has contributed more recent insights into pin-loaded FRP elements, particularly straps, loaded in tension—building upon Wörndle's earlier research [30]. Schürmann implemented a stress analysis based on force equilibrium principles, kinematic relations, and boundary conditions (the straps were assumed to be thick composite cylinders under internal pressure in their curved regions). Schürmann's findings highlighted the influence of the radius of curvature of the pins and the degree of orthotropy (longitudinal/transverse modulus) on the performance of straps—also noted by Mansfield [13]. Martin and Jackson [14,15] also investigated curved unidirectional (UD) laminates and cross-plied laminates under static loading, and revealed that the ultimate failure of these structures followed a complex progression; this includes the initiation of delamination due to radial stresses induced by bending and interlaminar tension (i.e. Mode-I) failure.

The first systematic investigations into pin-loaded laminated and non-laminated (thermoplastic matrix) CFRP straps were carried out by Winistörfer at Empa [16,17]. This research considered several potential manufacturing techniques, friction tests, an examination of stress concentration regions in tensioned straps, and an assessment of the influence of layer thickness for non-laminated straps, along with the impact of pin radius on strap performance in tension. Winistörfer also presented FE models of laminated, UD CFRP straps with steel pins (20 mm diameter, radius ratio: 1.3, friction coefficient: 0.2). It was demonstrated that the predicted failure location aligned with experimental results (i.e., failure was typically in the vertex area) and emphasized the critical nature of through-thickness normal and shear stress components, as compared with longitudinal stress [16].

Baschnagel et al. [18] further explored the effects of fretting on the tensile fatigue performance of CFRP straps intended for use as bridge hangars. In their work, they reported delamination as the consistent

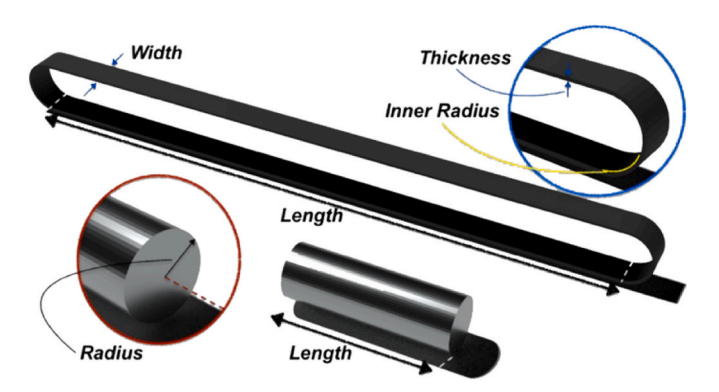


Fig. 1. Labelled features of the strap and pin used in the current study.

initial damage mode, originating at the ends of the inner overlapping zone of the strap and progressing toward the critical vertex area—ultimate failure of the strap was violent and sudden. It was experimentally observed that the failure region at the vertex area of the pin/strap contact interface was influenced by stress concentrations at that location. This was further verified by a simple three-dimensional one-eighth FE model of the pin/strap assembly (pin radius: 10 mm, strap thickness: 1 mm, strap width: 6 mm, friction coefficient: 0.5), where a local bending moment in the strap's curvature onset induced stress concentrations in the strap's vertex area (a phenomenon previously reported by Schürmann [11]).

The pin-loaded CFRP straps are unidirectional FRP tensile looped elements that are simple to anchor but have very anisotropic properties [11]. The main drawback is that, depending on the design of the looped end (e.g., radius of curvature, thickness, connection shape) and support conditions around the pin, their strength is reduced to 50%–70 % of the original strength of straight CFRP shafts. Therefore, it is crucial to understand the failure conditions of these pin-loaded CFRP straps using FEA models and validating with integrated DFOS for continuous strain profiling. This paper addresses these failure conditions. Thanks to their easy anchorage, corrosion resistance, and high fatigue resistance, CFRP elements are now used in Germany's first highly pretensioned network arch railway bridge (Stuttgart Stadtbahnbrücke over A8, Deutsche Bahn Oderbrücke Küstrin).

In the current paper, a numerical and experimental investigation of laminated, pin-loaded CFRP straps under tensile loading with the aim of understanding damage initiation, propagation, and failure is presented. Novel measurements are made using distributed fibre optics sensors based on Rayleigh backscattering—developed by LUNA Inc [19]. —were embedded within a pin-loaded CFRP strap (aligned parallel to the strap's fibre direction), enabling—for the first time—continuous strain monitoring in the curved area. Experimental results are compared with FE models incorporating the maximum stress criterion and with an analytical solution proposed by Schürmann [8]. The paper also further assesses the suitability of the different methods for failure prediction and the effectiveness/accuracy of the presented FE models.

2. Experimental details

2.1. Materials

The strap material used in the current study is a continuous UD carbon prepreg tape with IMS60 E13 24K 830tex fibres [20,31] with an Aradur Huntsman epoxy resin [21]. Titanium pins, made from Ti–6Al–4V alloy (Grade 5) [22], were supplied by CarboLink Ltd. in the form of cylindrical rods. The pin's length and radius were 62 \pm 2 mm and 10 \pm 0.1 mm, respectively (refer to Fig. 1).

2.2. Strap fabrication

Strap fabrication involved winding the carbon pre-impregnated tape around an aluminium mould six times and enclosing the assembly within a silicon belt and external aluminium clamps. The clamped assembly was then placed in an oven and cured for 2 h at 120 °C, followed by 1 h at 140 °C (heating rate: 3 °C/min), in accordance with the manufacturer's data sheet [21]. This resulted in straps that were 12 \pm 0.5 mm wide, 1 \pm 0.2 mm thick, and 250 \pm 0.5 mm long (see Fig. 1). Further details regarding strap manufacture are presented elsewhere [18,23,24].

2.3. Experimental Setup & methods

Six standard CFRP coupon specimens and six laminated CFRP straps underwent tensile testing at the Swiss Federal Laboratories for Materials Science and Technology (Empa) and at the University of Edinburgh to characterize their tensile mechanical properties. The coupon specimens

were tested using a Zwick 100 kN Machine equipped with a 100 kN load cell, while the CFRP straps were tested on an MTS Criterion C45.305 electromechanical loading frame fitted with a 300 kN load cell, as shown in Fig. 2a and b, respectively. The tensile tests were conducted in displacement control mode with a constant crosshead rate of 2 mm/min, following the ISO 527-4:2021 [25] and ISO 527-5:2009 standard test methods [26] for the coupon specimens and straps, respectively. The coupon specimens were extracted from the straight shaft length of the straps, then end-tabbed and tested until ultimate failure, with nominal dimensions of 250 \times 12 \times 1 mm (length \times width \times thickness). For the coupon specimens, crosshead measurements were recorded along with readings from an encoder (Zwick mutliXtens) that was additionally placed at the central region of the specimens. In the case of the straps, an AVX04 video extensometer system, using digital image correlation (DIC) and comprising an Allied Vision Manta G-146 camera, monitored the strain development in the mid-shaft region of the straps. Optical fibre strain sensors were additionally utilized for strain measurement.

Specifically, two types of optical fibres were used (see Fig. 3).

- An ormocer®-coated optical fibre containing spaced, low-reflective (R < 0.1 %) Draw Tower Gratings (DTGs®) supplied by FBGS®. This included 10 Fibre Bragg Grating (FBG) sensors with a 40 mm spatial separation, a 3 mm FBG length, and an 80 µm diameter, with a total length of 2.36 m. A Dynamic FBG-scan 804 interrogator (1510–1590 nm wavelength range, 4 optical channels) with built-in ILLumiSense® software was used, operating at a sampling rate of 100 Hz.
- A polyimide-coated optical fibre by FiberCore SM1250B3(9.8/125) with a 125 μm diameter allowed continuous local strain monitoring at a distance interval of 0.65 mm, using a LUNA ODISI 6104 DFOS Interrogator. The embedded distributed fibre optics sensors (DFOS) in the CFRP strap, aligned with the fibre direction, provided submillimeter strain measurement resolution and continuous strain profiles [27].

For clarity, the ply numbering indicating the sequence in which the strap was laid up around the mould is also shown in Fig. 3 (plies 1 to 6), i.e., ply-6 is the outermost ply of the continuously wound pin-loaded

strap.

3. Results and discussion

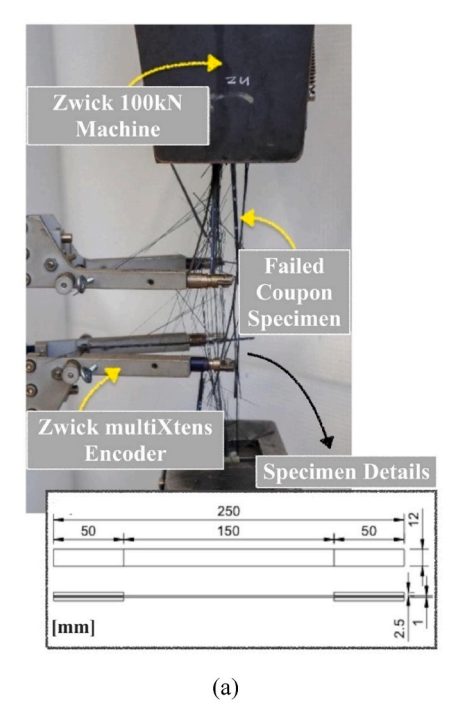
3.1. Tensile tests

A summary of the mechanical properties for the coupon specimens and the straps is given in Fig. 4. It should be noted that $F_{\text{max},1}$ (28.41 \pm 3.66 kN) corresponds to the load at which the straps' first visual delamination occurred. These results served as input parameters for an analytical solution by Schürmann which is discussed later in this paper.

The straps' longitudinal modulus (estimated following ISO 527-5 standard test method [26], based on which the strain values used were 0.05 % and 0.25 % with the corresponding stress values) is used in the FEMs of the pin/strap assembly described in the next sections (see Fig. 4c). Notably, the ultimate tensile strength (UTS) of the coupon specimens surpasses that of the straps by approximately 30 % (see Fig. 4b). This discrepancy is attributed to inherent differences in the specimen design wherein the straps include a curved vertex region, leading to stress concentrations that result in locally elevated stresses. Additionally, the overlap region, situated at the start and end points of the straps, is prone to delamination; as already noted, this is typically observed as the initial visual failure mode in such specimens; this is discussed in more detail in the next section.

3.2. Failure modes

Regarding the failure modes observed in both the coupon specimens and the straps, the typical sequence of failure was consistently observed and is outlined as follows: i) initial audible failures, characterized by minor incidents such as fibre breakages and matrix crack propagation; ii) subsequent visual detection of minor fibre breakages, primarily occurring towards the edges (of the clamped tabs in the coupons); iii) the occurrence of delamination events (noted exclusively in the case of the straps at the inner overlap end); iv) ongoing progression of delamination involving simultaneous audible and visible fibre breakages, either progressively or occurring simultaneously; and v) ultimate violent rupture. The coupon specimens ultimately failed within the free length,



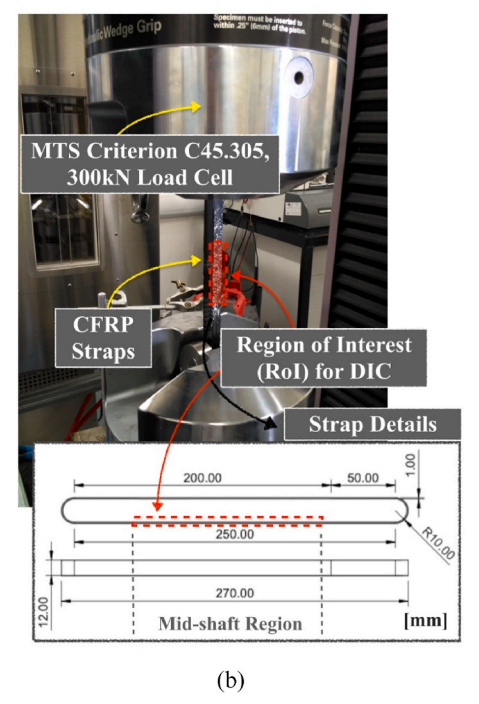


Fig. 2. Annotated test set-ups for (a) standard coupon specimens and (b) CFRP straps, along with specimen details.

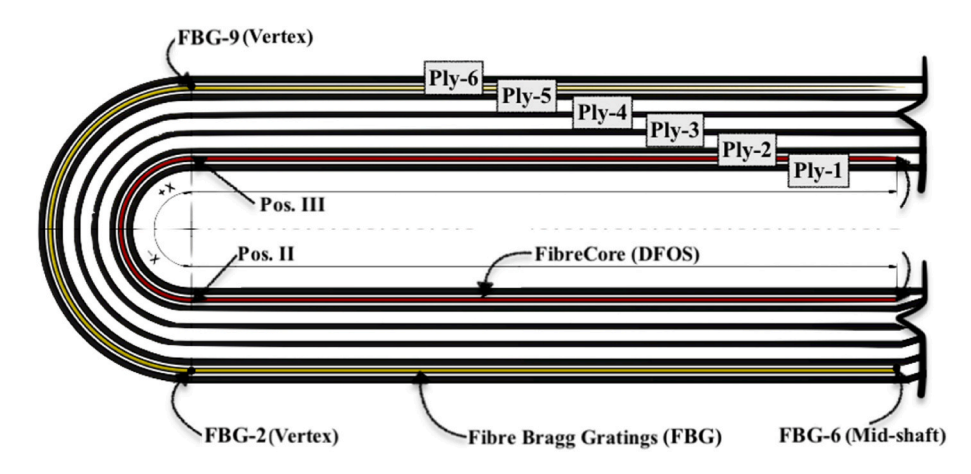


Fig. 3. Diagram of ply numbering, optical fibres (DFOS and FBG) within the strap, and locations for FBG strains.

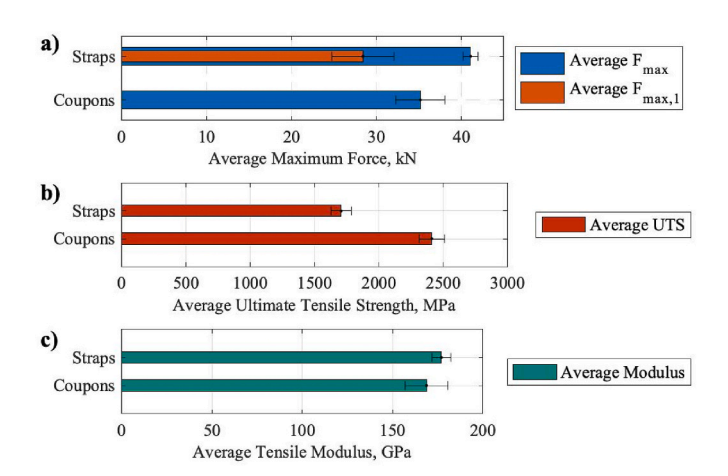


Fig. 4. Tensile properties of the coupon specimens and the straps tested: (a) Average maximum force (kN), (b) Average UTS (MPa), and (c) Average modulus (GPa)—error bars show standard deviations.

apparently starting from one clamped end (longitudinal splits and broken fibres were evident), while the straps ultimately failed at and around the vertex area (as also reported previously by others [18,24]).

3.3. Finite Element models

Finite Element models were created using SIMULIA Abaqus FEA (v2021) to analyse the tensile quasi-static behaviour of standard CFRP straps and examine key factors influencing their tensile performance. This section presents a one-eighth strap-pin FE model and a half strap-pin FE model—the latter of which serves to identify (delamination) failure initiation in specimens. Both the one-eighth and half FE models assumed identical material inputs in Abaqus and were subjected to displacement control in the longitudinal (i.e. 'y') direction (for enhanced computational efficiency and convergence), reaching approximately 38 kN of total reaction load at the pins (giving an average longitudinal stress in the shaft of approximately 1583 MPa). The "engineering constants" material type was chosen such that Young's moduli (E_1 , E_2 , E_3), Poisson's ratios (ν_{12} , ν_{13} , ν_{23}), and shear moduli (G_{12} , G_{13} , G_{23}) in the principal directions could be manually input.

Since the UD straps were considered as transversely isotropic materials, they could be represented with one axis of symmetry (along the fibre direction) [4]. Consequently, the elastic properties were simplified, employing five material constants: E_1 (longitudinal modulus), E_2 (transverse modulus), ν_{12} (in-plane Poisson's ratio), ν_{23} (out-of-plane Poisson's ratio), and G_{12} (in-plane shear modulus), with $E_2 = E_3$, $G_{12} = E_3$

 $G_{13}, \nu_{12}=\nu_{13}$, and $G_{23}=E_2/(2^*(1+\nu_{23}))$ (intralaminar shear modulus). The longitudinal and transverse modulus of the strap were obtained using the rule of mixtures (RoM) $E_{11}=V_fE_f+V_mE_m$ and the inverse rule of mixture (IRoM) $E_{22}=1/\left(\frac{V_f}{E_f}+\frac{V_m}{E_m}\right)$, respectively. The RoM was also applied to estimate the in-plane Poisson's ratio (ν 12), $\nu_{12}=V_f\nu_f+V_m\nu_m$. For predicting the in-plane shear modulus, the cylindrical assemblage model (CAM) was selected, $G_{12}=G_m\frac{(1+V_f)+(1-V_f)G_m/G_f}{(1-V_f)+(1+V_f)G_m/G_f}$, as it provides a more accurate predictions compared to the RoM [4].

The Poisson's ratio for the epoxy (ν_m) and the fibres (ν_f) was set at 0.35 and 0.25, respectively (epoxy vinyl ester, T700 fibres) [4], while the shear moduli of the fibres (G_f) and the matrix (G_m) were 42 GPa and 1.3 GPa, respectively [11]. The elastic modulus of the fibres in the axial direction (E_f) and the matrix (E_m) was based on available epoxy data and the fibres' data sheet $(E_f = 290 \text{ GPa } [20], E_m = 2.82 \text{ GPa})$. The elastic properties of the straps that were input in Abaqus are detailed in Table 1.

3.3.1. One-eighth FE model

The one-eighth model was expanded from a prior version (refer to Ref. [18]) which did not account for imperfections nor include failure criteria. In the current (updated) one-eighth model, the grips were incorporated within the model, to realistically assess potential bending—and shear deformations in the pins. The dimensions of the strap and pins used in the Finite Element (FE) analysis, where the one-eighth model is employed, are provided in Table 2. Notably, the modelled 'width' and 'shaft length' dimensions were half of the physical size of the straps (12 mm and 250 mm, respectively) since planar symmetry conditions have been applied. The modelled 'thickness' of the strap was 1 mm.

A diagram of the one-eighth FE model depicting the strap/pin assembly is illustrated in Fig. 5. In all analyses, both the strap and the pin were represented as 3D-solid deformable bodies, while the grips were modelled as analytical rigid bodies for computational efficiency (see details in Fig. 5). A reference point was designated on the grip, constraining all degrees of freedom for the rigid body, and serving as the point where displacement was applied in the y-direction. A composite layup was formulated using a single 1 mm thick ply, using the material properties provided in Table 1 and the material orientations shown in Fig. 5. A modulus and Poisson's ratio of 209 GPa and 0.30, respectively, were assigned to the titanium pin through a homogeneous isotropic

 Table 1

 Strap elastic properties used in FE models (moduli are presented in GPa).

E_1	E_2	E_3	ν_{12}	ν_{13}	ν_{23}	G_{12}	G_{13}	G_{23}
170.0	8.0	8.0	0.27	0.27	0.38	4.6	4.6	3.2

Table 2One-eighth FEM dimensions for the strap and the pin.

Strap Dimensions (mm)		Pin Dimensions (mm)	
Width	6	Pin Radius, R _{in}	10
Shaft Length	125	Length	10
Inner Radius, Rin	10		
Outer Radius, Rout	11		

section (extracted from the supplier's data sheet). Planar symmetry boundary conditions were applied in the one-eighth FE model (x-symmetry, y-symmetry, z-symmetry) where appropriate—i.e. at the edge faces of the strap and pins (refer to Fig. 5).

A surface-to-surface contact interaction with a finite sliding formulation was chosen to accommodate the friction between the strap and the pin, with the friction coefficient set at 0.5 (in accordance with [18]). Fig. 6 displays a stress distribution in the one-eighth FE model, showcasing stress patterns akin to the model developed by Baschnagel et al. [18]. Notably, the titanium pin exhibits a high degree of rigidity, displaying minimal bending deformation when in contact with the strap, given the high shear strength and stiffness of the titanium pin.

3.3.2. Half FE model

A Python script was written to automate the generation of the half model for the pin/strap assembly, as illustrated in Fig. 7. To initiate the

script, the user inputs values for various parameters, including the number of plies, distance between titanium pins, pin radius, material properties, applied displacement, and mesh settings for both pins and the strap. The dimensions employed in the half model align with those outlined in Table 2, except that the shaft length (equivalent to the distance between the two pins) was set to 250 mm rather than 125 mm. For the input, six plies were specified, corresponding to a 1 mm thick strap. Each individual ply consisted of two components that were subsequently tie-constrained (to each other and to neighbouring plies), simulating the continuous prepreg tape wrapped around the aluminium mould. The composite lay-up and material orientation matched those of the one-eighth model, as shown in Fig. 5.

The pins and the strap were meshed (at the beginning of the script) with a global mesh density of 0.6 and 0.8, respectively, and the strap was seeded with 40 elements around the curvature. Similar to the one-eighth model, C3D8 elements were employed, and across the width of the strap, 12 elements were distributed, with each ply consisting of a single element through its thickness. A general contact interaction was assigned to the whole model with two contact properties: i) a global contact property with a coefficient of friction of 0.5 between the parts; and ii) a cohesive contact property applied exclusively to the surfaces between each of the plies, with a shear strength of 30 MPa and interlaminar strength of 45 MPa (strengths based on [21]).

The half model did not consider damage evolution, and symmetry boundary conditions, consistent with those of the one-eighth model,

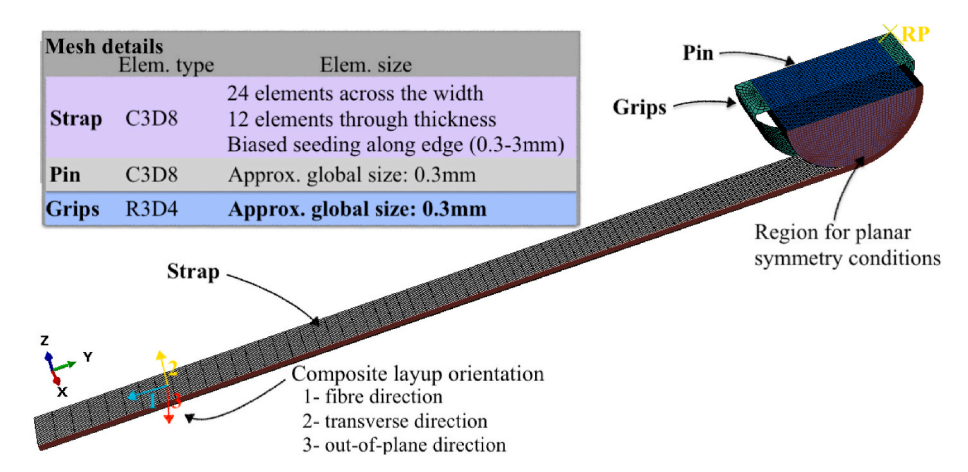


Fig. 5. One-eighth FE model with mesh, symmetry conditions and material orientation details.

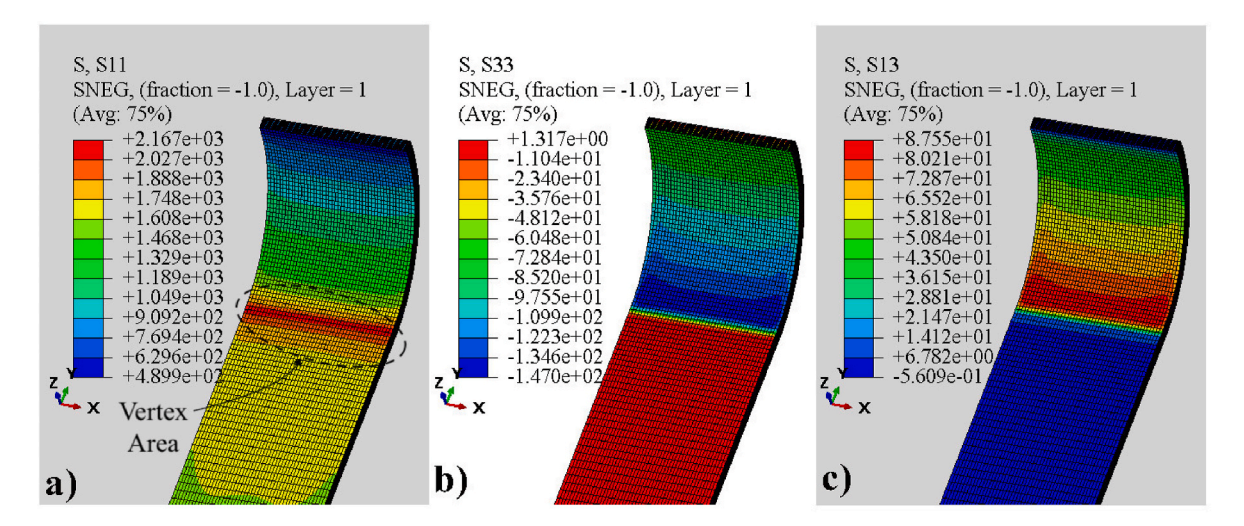


Fig. 6. Stress distribution (MPa) for an applied displacement corresponding to a total load for the complete strap of 38 kN in the (a) longitudinal, (b) out-of-plane normal, and (c) out-of-plane shear direction using a titanium pin.

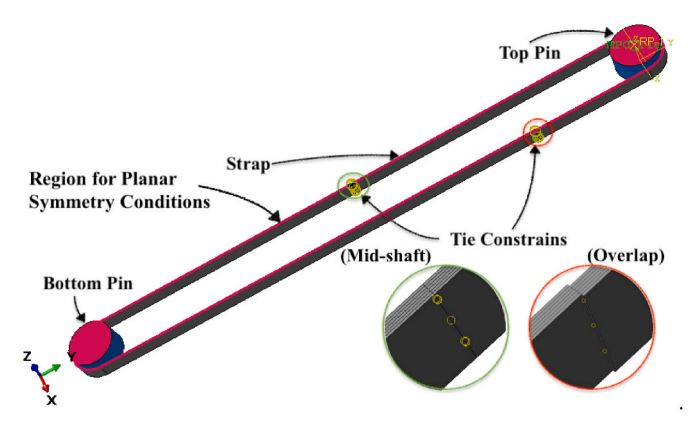


Fig. 7. Half FE model with locations of tie constraints and region of planar symmetry conditions.

were employed. Displacement was applied at the reference point (RP), which was multi-point constrained (MPC) on one side to the top pin in the Y-direction (see Fig. 7). The resulting stresses and contact stress ratios in the overlap region are shown in Fig. 8. It should be noted that

the overlap region was 50 mm away from the upper vertex area (refer to Fig. 8) to align with the lay-up of the straps. Additionally, Fig. 8e and f presents the results of a mesh convergence analysis for the overlap region. The number of longitudinal element seeds along the straight lengths between the vertex areas and overlap region were defined by dividing these distances (e.g., 50 mm from the upper pin and 200 mm from the lower pin) by denominator values of 1, 0.5, 0.25, 0.125, and 0.0833—see Fig. 8e. A seeding bias of 5.0 was applied in all simulations, increasing the mesh density towards the overlap region. In Fig. 8f, the predicted damage onset loads are plotted for cases where 1, 2, and 3 (through thickness) elements per ply were considered. For all variations, the predicted delamination initiation loads were within 2.45 % of the baseline value. The use of cohesive interfaces was deemed a suitable method for approximating damage onset in the half FE model based on the results of this convergence analysis.

The stresses in the longitudinal direction exhibit around 32 % higher values compared to the one-eighth FE model (and [18]), which is reasonable considering that each ply has an individual stress profile (interacting via cohesive zone). The stresses in the out-of-plane normal and shear directions (Fig. 8b and c) follow similar distributions as in the one-eighth FE model, with approximately a 19 % increase and a 27 % decrease in the respective stresses. By employing a cohesive zone

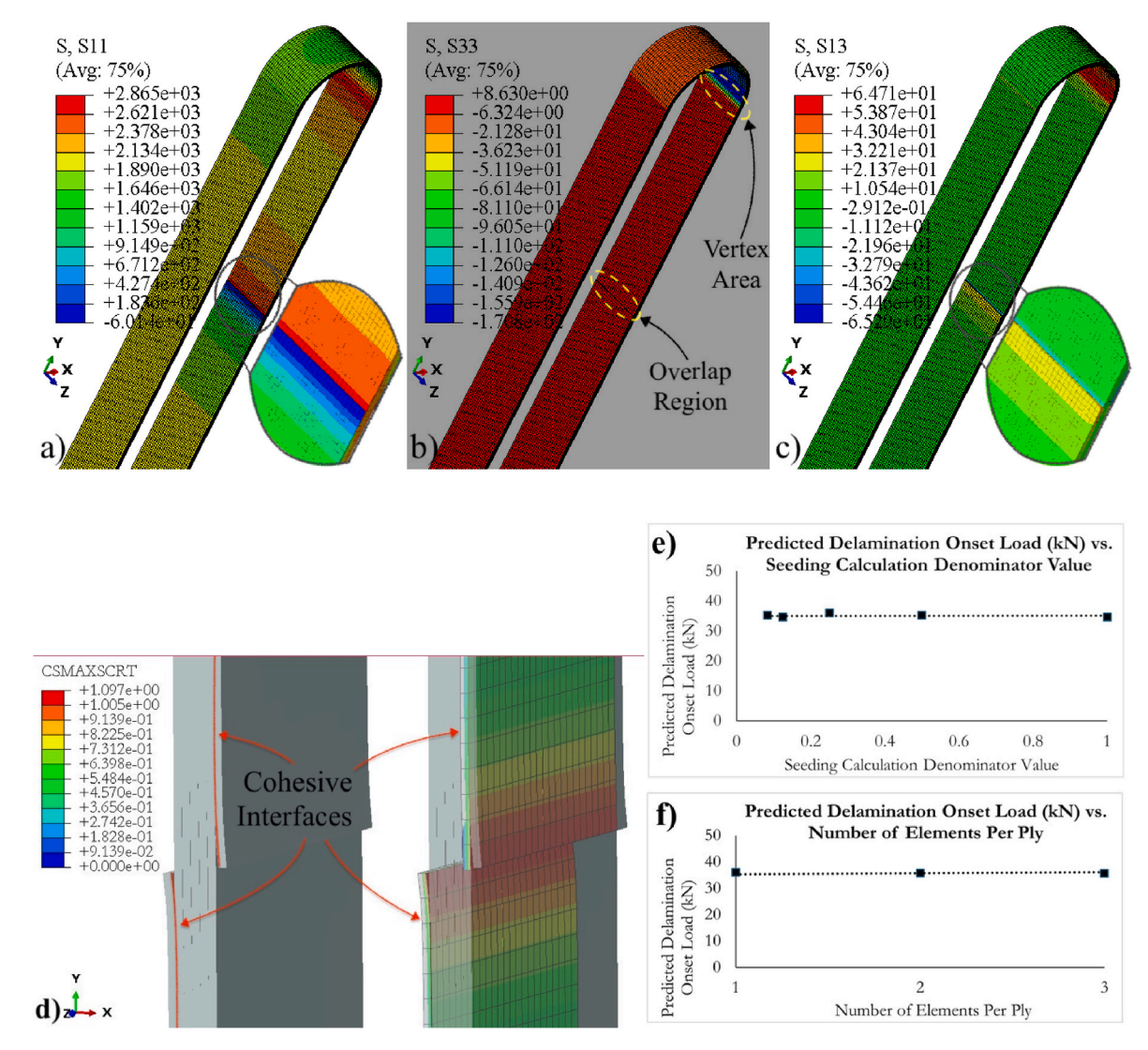


Fig. 8. Stress distributions for an applied displacement corresponding to a total load for the complete strap of 38 kN in the (a) longitudinal direction, (b) out-of-plane normal direction, (c) out-of-plane shear direction, and (d) contact stress ratio within the cohesive zone for the maximum stress criterion at the overlap region. (e) Predicted delamination onset load versus seeding calculation denominator value. (f) Predicted delamination onset load versus number of elements per ply.

between the plies, it was possible to examine the contact stresses and the stress ratios at which delamination occurred. In Fig. 8d (left), the maximum stress criterion of the cohesive elements on the outer plies of the overlap region is shown. Here, the stress ratio surpasses 1.0, indicating that delamination has occurred at the surfaces shown (at around 35 kN) which is reflected by the numerical values of the contact stress ratio in Fig. 8d (right).

3.3.3. Load at failure

Two failure criteria were used in this work: the maximum stress criterion [28] (Eq. (1)) and a fibre (specific) failure criterion proposed by Puck and Schürmann [11] (Eq. (2)). In each case, the resultant stresses from the one-eighth and half model, respectively, were implemented in the criteria to predict the load at which first failure is more likely to occur. The equations that describe each criterion are:

$$X_T \le \sigma_1 \text{ or } \sigma_1 \le X_C, \sigma_2 \ge Y_T \text{ or } \sigma_2 \le Y_C, |\sigma_{12}| \ge S_{12}$$
 Equation 1

$$\delta_{S} = \left| \frac{1}{R_{\parallel}^{\pm}} \left[\sigma_{1} - \left(\nu_{12} - \nu_{f} \frac{E_{11}}{E_{f}} m_{f} \right) (\sigma_{2} + \sigma_{3}) \right] \right| = 1 \begin{cases} R_{\parallel}^{+}, for \left[\dots \right] \geq 0 \\ R_{\parallel}^{-}, for \left[\dots \right] \leq 0 \end{cases}$$

Equation 2

In Eq. (1), failure occurs once one of the stress conditions is met. X_T and X_C are the ultimate tensile (UTS) and compressive strength, respectively. Y_T and Y_C are the transverse tensile and compressive strength, respectively, and S_{12} is the shear strength. σ_1 , σ_2 , and σ_{12} , longitudinal, transverse, and shear stresses, respectively, derived from the FE model. The values used for X_T , X_C , Y_T , Y_C , and S_{12} are 2412 MPa, 1800 MPa, 30 MPa, 84 MPa, and 68 MPa, respectively. These strength assumptions are based on available VTC401 properties and [11,21,28].

In Eq. (2), the symbols represent the following: R_{\parallel}^{\pm} , the theoretical ultimate tensile (+)/compressive (-) strength; σ_1 , σ_2 , and σ_3 , longitudinal, transverse, and out-of-plane normal stresses, respectively, derived from the FE model; ν_{12} and ν_f , in-plane (0.27, refer to Table 1) and fibre Poisson's ratio (0.1, see Ref. [20]), respectively; E_{11} and E_f , longitudinal (170 GPa, refer to Table 1) and fibre (290 GPa, see Ref. [20]) elastic modulus, respectively; m_f , the magnification factor accounting for the strain mismatch between stiff fibres and the matrix, resulting in a non-uniform transverse stress distribution. Schürmann [11] suggests the empirical value of $m_f = 1.1$ for carbon fibres. Concerning the ultimate tensile strength, the theoretical value of 2412 MPa was used in Eqs. (1) and (2), based on coupon tensile tests (see Fig. 4). This theoretical UTS of 2412 MPa aligns reasonably well with the value reported by Meier et al. [29], where IMS60 fibres ($V_f = 60$ %) were also used (2130 MPa).

The stresses were extracted around the vertex area (closer to the outer edge of the strap) in both the one-eighth and half FE models (see dashed circled areas in Figs. 6a and 8b and blue-marked region in Fig. 10d). The stresses utilized in the equations are presented in Fig. 9 for (a) the one-eighth and (b) the half FE model, respectively. Fig. 9b, also includes the contact stress ratio for the cohesive zone at the overlap region (CS Ratio) of the half FE model; when the ratio exceeds 1.00, it indicates delamination has occurred. The corresponding damage limit (δ_S) of Schürmann's criterion (Eq. (2)), which signifies that when the damage limit is at or above 1.0 failure has occurred in the investigated region, is also shown in Fig. 9.

Utilizing linear interpolation, the load corresponding to the first fibre failure in the one-eighth model (Eq. (1); $\delta_S=1.0$) was determined to be 42.13 kN, with the associated stresses at the vertex being $\sigma_I=2393.3$ MPa, $\sigma_2=-3.99$ MPa, and $\sigma_3=-87.22$ MPa (refer also to Fig. 9a). For the half model, failure appears to occur around 41.12 kN, with the corresponding stresses at the vertex being $\sigma_I=2390.5$ MPa, $\sigma_2=-0.86$ MPa, and $\sigma_3=-103.98$ MPa. In Fig. 4, the experimental load at which fibre breakage occurs for the straps is 41.09 \pm 0.88 kN. Comparing this experimental value with the predicted values of 42.13 kN and 41.12 kN from the failure criterion based on the one-eighth and the half models,

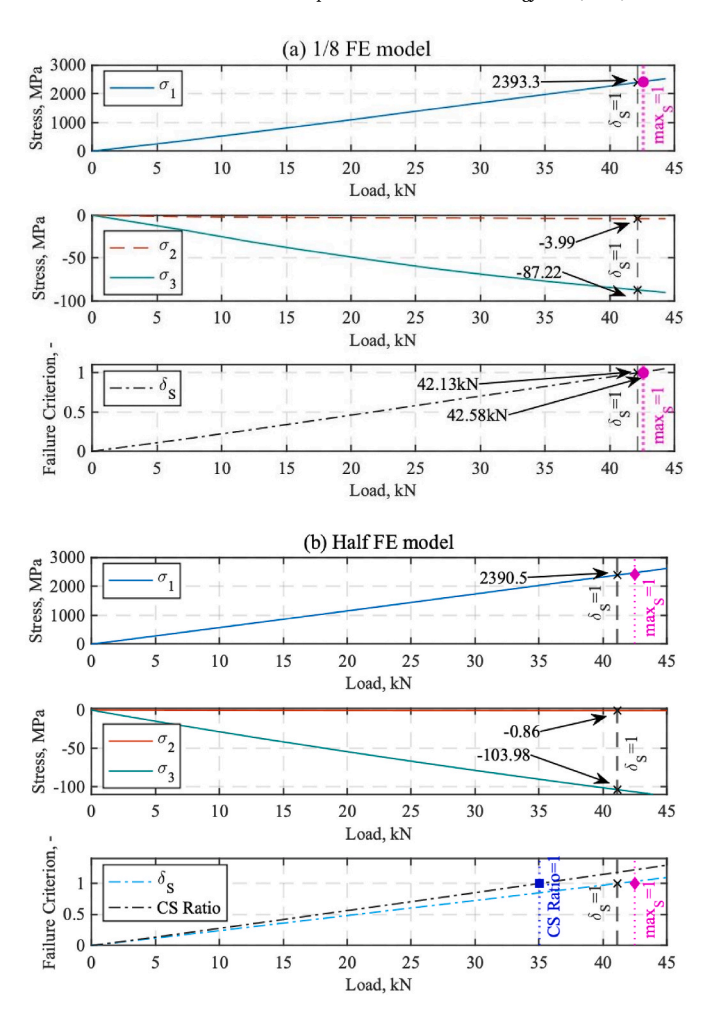


Fig. 9. (a) Resultant stresses $(\sigma_1, \sigma_2 \text{ and } \sigma_3)$ from the one-eighth FE model and the damage limit for Schürmann's criterion (δ_s) along with the max stress criterion (\max_s) . The stresses when the failure criterion is met and the load at which first fibre failure occurs are shown with arrows. (b) Resultant stresses $(\sigma_1, \sigma_2 \text{ and } \sigma_3)$ from the half FE model, damage limit for Schürmann's criterion (δ_s) and max stress criterion (\max_s) , and contact stress ratio (CS Ratio) for the cohesive zone at the overlap region along with the corresponding load when delamination occurs.

respectively, indicates excellent prediction accuracy (0.073–2.5 % difference). However, the one-eighth model does not account for the overlap of the plies, which the half model does. In the latter, stresses around the overlap region of the strap are significant, and it has been established experimentally that this is where the first visual (fibre) failure occurs. Referring to the last plot in Fig. 9b, the predicted value at which delamination occurs in the half model (CS Ratio is 1.00) is 35.02 kN. In Fig. 4, the first visual delamination of the straps occurs at 28.41 \pm 3.66 kN. This discrepancy is reasonably reconciled by considering the standard deviation, with a maximum difference of around 9.2 %.

When applying the maximum stress criterion, reaching the stress condition in Eq. (1) corresponds with the Ultimate Tensile Strength (UTS), signifying tensile failure in the longitudinal (fibre) direction where the stress exceeds 2412 MPa. The failure loads for the one-eighth and half models (where $\sigma_1=$ UTS = 2412 MPa) were 42.58 kN and 41.48 kN, respectively (see Fig. 9). Upon comparing these results with experimental data, the maximum stress criterion appears to accurately predict the load at failure, demonstrating an approximately 3.4 % difference for the one-eighth model and around 0.95 % for the half model. The slightly lower difference in the half model may be attributed to its increased complexity, as it considers the interaction between plies and suggests delamination occurs at an earlier stage. In summary, both

criteria exhibit reasonable predictive accuracy for the first failure load when compared against experimental outcomes.

3.3.4. Strain comparison between FE analyses and optical fibre sensors

The longitudinal strains obtained from the Finite Element (FE) analyses employing a titanium pin as discussed in Sections 3.3.1 1/8 FE Model and 3.3.2 Half FE Model, are compared with optical fibre measurements taken during (experimental) tensile testing. The positioning of the optical fibres and gratings was detailed in Section 2.2 Experimental Methods. In Fig. 10a-c, the longitudinal strains in the vertex area (FBG-2, FBG-9, and DFOS) and in the midshaft region (FBG-6 and DFOS) during tensile testing are compared to the corresponding strains obtained through the FE models. The strains from both the one-eighth and the half models were extracted from the elements at the vertex area of the strap nearer to the region where the symmetry conditions were applied, as shown in Fig. 10d since both the optical fibres were placed near the middle of the strap. The locations for extracting stress and strain from the models were selected to align with the 3 mm length of the FBG, and thus the plotted strains and stresses in Fig. 10a-c are the average strain and stress values extracted from the models (refer to Fig. 10d). With respect to Fig. 10c, the strains and stresses were extracted from the mid-shaft region of the straps in a manner similar to that employed for

Average FEM strains appear to align reasonably well with the Fibre Bragg Grating (FBG-2 and FBG-9) and the Distributed Fibre Optic Sensor (DFOS) strains at the vertex area of the straps, as depicted in Fig. 10a and b. In the mid-shaft region, where stress and strain experimental measurements were available (strains obtained with Digital Image Correlation (DIC) analysis, as shown in Fig. 10c), the stress versus strain response of FBG-6, DFOS and DIC measurements are compared to the FE analyses. The stress versus strain curves in Fig. 10c reveal that both FE models' response closely matched the experimental results, indicating their ability to reasonably predict the straps' responses. This alignment is partly attributed to the 'quasi-continuous' distributed measurement

technique of the DFOS. Findings suggest that although the one-eighth model lacks sophistication (with no overlap modelling or failure criteria), it reasonably predicts the tensile response of the straps. However, the need to implement the half FE model becomes apparent when comparing the results at the vertex area, particularly focusing on the localized strains between the first two plies that are in close contact with the titanium pin. The use of DFOS allows for a strain comparison with the half FE model at different load levels along the entire length of the embedded optical fibre—something not feasible with the FBG sensors since they were 40 mm apart within the optical fibre. This is illustrated in Fig. 11, where strains obtained from the half FE model along the strap's symmetry at 10, 20 and 25 kN load levels are additionally plotted. Strains were not extracted from the half FE model beyond 25 kN due to the absence of damage progression. This decision was based on

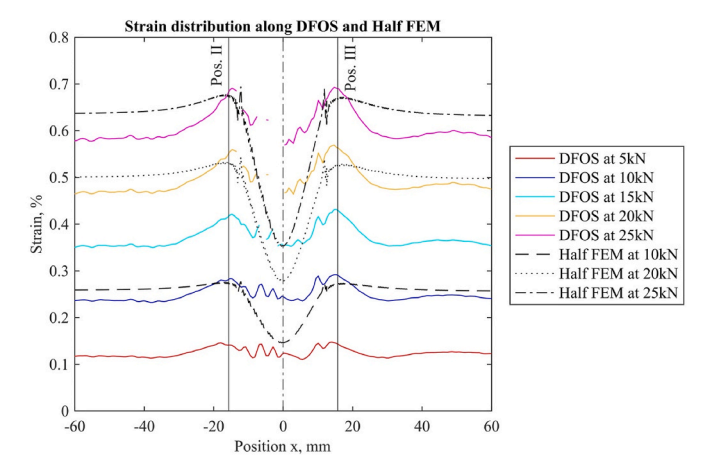


Fig. 11. DFOS and half FEM longitudinal strain distribution around and near the vertex area at different load levels.

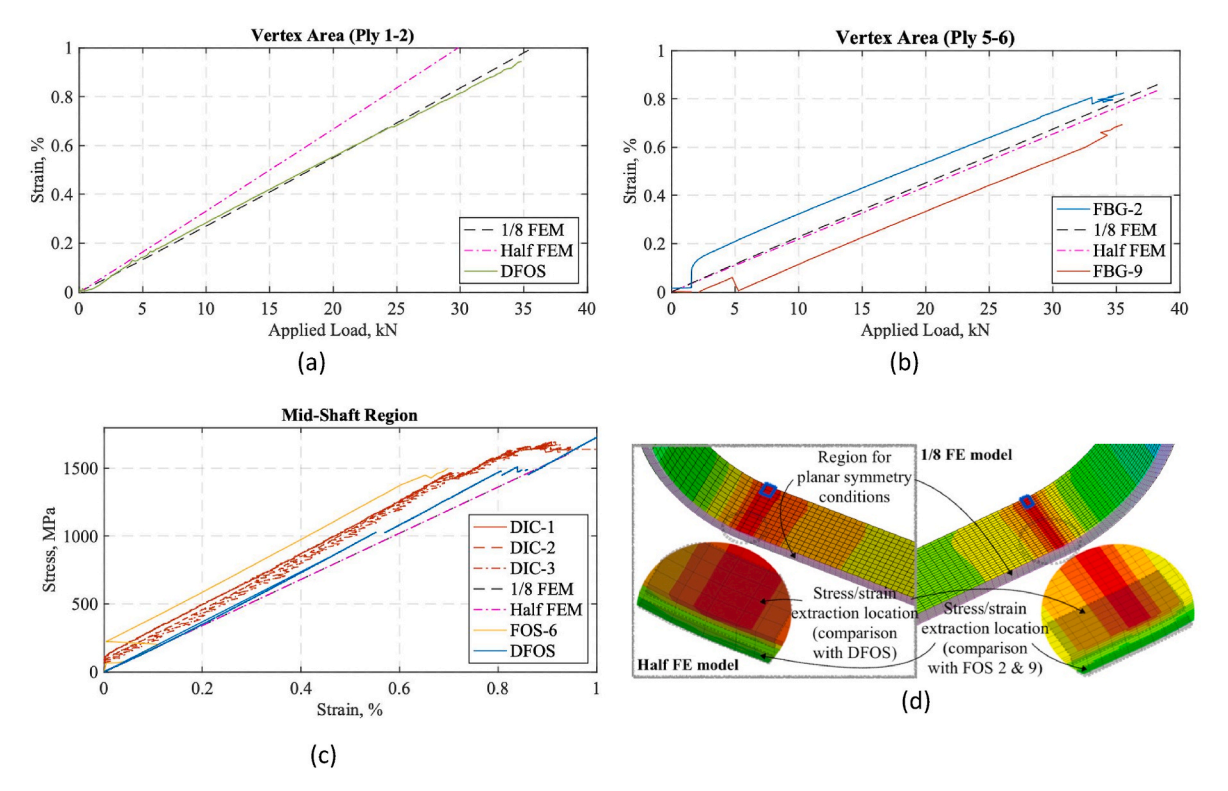


Fig. 10. Strains versus applied load at the vertex area between: (a) the first and second ply, and (b) the fifth and sixth (last) ply. (c) Stress versus strain at the midshaft region obtained with both optical fibres, the one-eighth FE model, the half FE model and the DIC. (d) Stress and strain extraction locations from the one-eighth and the half FE models (blue region used for comparison with strength-based failure criterion).

experimental observations indicating that delamination typically occurred at about 28 kN (see Fig. 4). Fig. 11 also shows the location of the vertex regions of the embedded DFOS chord (Pos. II and Pos. III) to aid in interpreting the results.

The peak strain values around the vertex areas of the half FE model coincide well with the DFOS readings at and around Pos. II and Pos. III. At these points, theoretically, no transverse pressure is present, and the measurement quality not compromised. Specifically, the peak strains obtained from the half FE model at 10 kN load level are approximately 4.02 %–9.44 % lower when compared to the DFOS strains at 10 kN; while at 20 kN they are around 2.04 %–6.63 % lower compared to the DFOS strains. A slightly greater disparity is observed in the strain peaks at a 25 kN load level between the DFOS and the half FE model (approximately 0.45 %–10 % higher strains exhibited by the half FE model). One reason for this behaviour can be attributed to mesh dependencies and input parameters used.

Another noteworthy observation is the different strain distribution within the curved region of the strap (between Pos. II-III), where the strains from the half FE model are lower compared to the DFOS readings. A possible explanation for this strain mismatch is the effect of high radial pressure, leading to transverse compression of the optical fibre. The LUNA ODiSI 6104 interrogator used in this study usually allows strain measurement up to 1.5 % under the assumption of a reasonably smooth strain distribution and non-existent transverse pressure. However, in the curved region, where transverse pressure acts, correlation is partially lost even at strains of 0.4 % (which corresponds to a radial pressure of about 38 MPa). The lower strain values between Pos. II-III obtained from the half FE model could be attributed to mesh dependencies (a much finer mesh might be necessary) and to the coefficient of friction (0.5). Another reason could be that the half FE model doesn't account for any progressive damage mechanisms or load redistribution. Overall, the half FE model predicted the strain distributions around the critical vertex areas well when compared to the DFOS, with some expected variations between experimental and simulation data as discussed above (up to 9.4 % difference).

4. Conclusions

This paper has investigated the quasi-static tensile performance of titanium pin-loaded carbon fibre reinforced polymer (CFRP) straps through a combination of experimental and numerical analyses. Specifically, a one-eighth Finite Element (FE) model and a half model of the pin/strap assembly were developed, and their resultant strain, stress, and applied load at different regions were compared against experimental data obtained via digital image correlation (DIC) and optical fibres—fibre Bragg grating (FBG) and distributed fibre optic sensor (DFOS)

The findings indicate that both FE models effectively captured the local strain development around the vertex area and the mid-shaft region of the strap, exhibiting good agreement with DIC, FBG, and DFOS readings. When comparing the strain distributions along the DFOS length to that of the half FE model around and at the vertex area, the half FE model deviated slightly (up to 10 % difference), primarily within the straps' curved regions. Possible reasons for this strain mismatch were attributed to high transverse pressures around the curved region and potential mesh dependencies of the half FE model. The influence of the transverse pressure on DFOS-measurements in such situations represents a novel insight and should be further investigated in the future.

In comparing the load at failure obtained from experiments, the oneeighth, and half FE models to Schürmann's analytical solution and the maximum stress criterion, it was observed that both criteria could reasonably predict the first failure load when compared with the experimental results (<2.5 % difference). Furthermore, the value at which delamination (first visual failure of the strap) occurred in the half FE model (CS Ratio is 1.00) was in reasonable agreement with the experimental values, particularly when considering the experimental standard deviation—approximately 9.2 % (maximum).

CRediT authorship contribution statement

Danijela Stankovic: Writing – review & editing, Writing – original draft, Visualization, Validation, Methodology, Investigation, Formal analysis, Data curation, Conceptualization. James R. Davidson: Writing – review & editing, Visualization, Validation, Formal analysis, Data curation. Valentin Ott: Writing – review & editing, Methodology, Investigation, Formal analysis, Data curation, Conceptualization. Luke A. Bisby: Writing – review & editing, Validation, Supervision, Resources, Project administration, Funding acquisition, Conceptualization. Giovanni P. Terrasi: Writing – review & editing, Validation, Supervision, Resources, Project administration, Funding acquisition, Conceptualization.

Declaration of competing interest

The authors declare that they have no known competing financial interests or personal relationships that could have appeared to influence the work reported in this paper.

Acknowledgements

This work has been funded by the Swiss Federal Laboratories for Materials Science and Technology (Empa) and University of Edinburgh studentship CT-5126 (2017).

Data availability

Data will be made available on request.

References

- P.T. Curtis, Fatigue * *Crown copyright, in: Mechanical Testing of Advanced Fibre Composites, Elsevier, 2000, pp. 248–268.
- [2] V.V. Vasiliev, E.V. Morozov, Mechanics of a unidirectional ply, in: Advanced Mechanics of Composite Materials, Elsevier, 2013, pp. 53–124.
- [3] L.A. Carlsson, D.F. Adams, B.R. Pipes, Experimental Characterization of Advanced Composite Materials, fourth ed. ed., CRC Press, Boca Raton, 2014.
- [4] E.J. Barbero, Introduction to Composite Materials Design, third ed., CRC Press, 2017.
- [5] H.T. Hahn, Fatigue behavior and life prediction of composite laminates. ASTM. Composite Materials: Testing and Design (Fifth Conference), 1979, pp. 383–417.
- [6] Composite Materials Handbook. Volume 1. Polymer Matrix Composites Guidelines for Characterization of Structural Materials, 2002. Washington.
- [7] Z. Hashin, Failure criteria for unidirectional fiber composites, J. Appl. Mech. 47 (June 1980) 329–334.
- [8] A. Puck, H. Schürmann, Failure analysis of FRP laminates by means of physically based phenomenological models, Compos. Sci. Technol. 62 (2002) 1633–1662.
- [9] S.T. Pinho, C.G. Davila, P.P. Camanho, L. Iannucci, P. Robinson, Prediction of Compression Strength of Unidirectional Polymer Matrix Composites, 2005.
- [10] A.C. Orifici, I. Herszberg, R.S. Thomson, Review of methodologies for composite material modelling incorporating failure, Compos. Struct. 86 (2008) 194–210.
- [11] H. Schurmann, Konstruieren mit Faser-Kunststoff-Verbunden, Springer Berlin Heidelberg, Berlin, Heidelberg, 2007, pp. 393–439.
- [12] A. Puck, H. Schürmann, FAILURE ANALYSIS OF FRP LAMINATES BY MEANS OF PHYSICALLY BASED PHENOMENOLOGICAL MODELS1This article represents the authors' contributions to a world-wide exercise to confirm the state-of-the-art for predicting failure in composites, organised by Hinton and Soden.[24]1, Compos. Sci. Technol. 58 (1998) 1045–1067.
- [13] E.H. Mansfield, Load transfer from a pin to a wound fibre composite strip, Procurement Executive, Ministry Of Defence. Aeronautical Research Council Reports and Memoranda (1977) 1–35.
- [14] R.H. Martin, Delamination Failure in a Unidirectional Curved Composite Laminate, 1990.
- [15] R.H. Martin, W.C. Jackson, Damage prediction in cross-plied curved composite laminates, in: W.W. Stinchcomb, N.E. Ashbaugh (Eds.), Composite Materials: Fatigue and Fracture, West, Conshohocken, vol. 4, ASTM International, 1993, pp. 105–126.
- [16] A.U. Winistörfer, Development of Non-laminated Advanced Composite Straps for Civil Engineering Applications, 1999.
- [17] A. Winistörfer, U. Meier, CARBOSTRAP-An advanced composite tendon system, in: FRPRCS-5: Fibre-Reinforced Plastics for Reinforced Concrete Structures, vol. 1, 2001, pp. 231–238.
- [18] F. Baschnagel, Fretting Fatigue Behaviour of Pin-Loaded CFRP Straps, 2015.

- [19] I. Luna, Advanced Fibre Measurement and Monitoring Systems, 2023.
- [20] TEIJIN Toho Tenax^(®) Europe GmbH," Kasinostraße 19-21, 42103 Wuppertal, Germany.
- [21] Huntsman Advanced Materials GmbH," Klybeckstrasse 200, 4002 Basel, Switzerland.
- [22] Titanium Grade 5," Narrowboat Way, Hurst Business Park, Brierley Hill, West Midlands, DY5 1UF UK.
- [23] D. Stankovic, L.A. Bisby, G.P. Terrasi, Influence of temperature on the mechanical performance of unidirectional carbon fiber reinforced polymer straps, Materials 14 (April 2021) 1903.
- [24] D. Stankovic, L.A. Bisby, Z. Triantafyllidis, G.P. Terrasi, Fretting fatigue performance of unidirectional, laminated carbon fibre reinforced polymer straps at elevated service temperature, Polymers 13 (October 2021) 3437.
- [25] Plastics Determination of Tensile Properties Part 4: Test Conditions for Isotropic and Orthotropic Fibre-Reinforced Plastic Composites, 2021. UK.

- [26] Plastics. Determination of Tensile Properties. Part 5: Test Conditions for Unidirectional Fibre-Reinforced Plastic Composites, 2009. UK.
- [27] A. Hehr, M. Norfolk, J. Sheridan, M. Davis, W. Leser, P. Leser, J.A. Newman, Spatial strain sensing using embedded fiber optics, J. Occup. Med. 71 (January 2019) 1528–1534.
- [28] V.V. Vasiliev, E.V. Morozov, Failure criteria and strength of laminates, in: Advanced Mechanics of Composite Materials, Elsevier, 2007, pp. 321–357.
- [29] U.O. Meier, A.U. Winistörfer, L. Haspel, World's first large bridge fully relying on carbon fiber rein-forced polymer hangers, in: SAMPE Conference 2020 Amsterdam, 2020.
- [30] R. Wörndle, W. Daschner, Rechnerische Untersuchung von zug- und druckbelasteten FVW-Strangschlaufen. (EN) Calculation of tension and compression loaded strand loops of fibre reinforced plastics, Z. für Flugwiss. Weltraumforsch. 1 (1980) 38–47.
- [31] Toray Composite Materials America, Inc," 19002 50th Avenue East, Tacoma, WA 98446.